Acoustic and Performance Characteristics of an Ideally Twisted Rotor in Hover

Nicole A. Pettingill, * Nikolas S. Zawodny, † Christopher S. Thurman, ‡ and Leonard V. Lopes §
NASA Langley Research Center, Hampton, VA, 23681

A series of experiments were conducted in an anechoic chamber to investigate the noise and performance of an ideally twisted rotor design, leading to validation of a low-fidelity aerodynamic performance and acoustic modeling tool chain. An "ideally twisted" rotor was designed in order to simplify the theoretical rotor inflow for a target thrust condition in hover. This rotor design was then fabricated using state-of-the-art rapid prototyping and tested in an anechoic chamber. Aerodynamic load and acoustic data were acquired across a range of rotation rates and rotor collective settings in order to both identify noise trends and ascertain the accuracy of the low-fidelity modeling codes. Emphasis was placed on modeling of the broadband self-noise generated by the rotor system due to the fact that it was found to be a prominent contributor to the overall rotor system noise.

Nomenclature

English

A_0	Rotor collective angle, deg.
c	Chord length, m
C_T	Thrust coefficient, $\frac{T}{\rho\pi\Omega^2 R^4}$
H	Trailing edge bluntness thickness, m
M_{tip}	Tip Mach number
N_b	Number of rotor blades
Q	Torque, N $\cdot$ m
r	Spanwise location from hub, m
R	Blade radius, m
St	Strouhal number relative to bluntness thickness, $\frac{f * H}{U_{tip}}$
T	Thrust, N
U_{tip}	Tip speed, m/s

Greek

α	Local aerodynamic angle of attack, deg.
$\theta_\circ$	Observer angle, deg.
Θ	Blade pitch angle as measured from the root, deg.
Θ_{tip}	Blade tip pitch angle, deg.
σ	Rotor solidity, $\frac{N_b * c}{\pi R}$
ϕ	Local induced angle, deg.
Ω	Rotation rate, RPM

Subscript

bb	Broadband noise
bb, pr	Broadband noise with tonal peaks removed

*Research Aerospace Engineer, Aeroacoustics Branch, AIAA Member; nicole.a.pettingill@nasa.gov
†Research Aerospace Engineer, Aeroacoustics Branch, AIAA Member; nikolas.s.zawodny@nasa.gov
‡Research Aerospace Engineer, Aeroacoustics Branch, AIAA Member; christopher.thurman@nasa.gov
§Senior Research Aerospace Engineer, Aeroacoustics Branch, AIAA Member; leonard.v.lopes@nasa.gov

c	Corrected rotation rate (for sea level, standard day conditions)
max	Highest rotation rate condition
$mech$	Mechanical rotation rate
tip	Tip condition

I. Introduction

Over the past decade, the emergence of small Unmanned Aircraft Systems (UAS) and Advanced Air Mobility (AAM) vehicles has shown to have the potential to redefine the airspace. The acoustic characterization of small rotor blades is important due to their applicability to small UAS, and potentially to larger Urban Air Mobility (UAM) vehicle platforms. Low-fidelity acoustic tools are often being used to predict the noise from these vehicles and must be assessed to further verify their accuracy for usage in the vehicle design process. This paper provides validation and identifies limitations of the current low-fidelity noise prediction toolset. Validation data were collected through a set of hover chamber experiments. Prior experimental studies of small-scale rotors in hover have been performed with commercial off the shelf (COTS) rotors [1, 2]. With COTS rotors, it is not always possible to know the exact geometric properties or the complexity of the inflow.

A rotor with an ideal twist distribution theoretically has uniform inflow, which may be simpler to predict using low-fidelity tools. The predictions in this paper focus on harmonic content and broadband self-noise; however, additional broadband noise sources are present in the experiment that cannot be modeled with the current low-fidelity tools. These additional noise sources, primarily blade wake interaction (BWI) noise and turbulence ingestion noise (TIN), have been identified by Ref. [3]. The toolset methodology used for this paper is similar to the broadband prediction methodology that has been employed in previously published predictions of small rotors, such as in Ref. [4]. The experimental work and predictions in this paper have helped with understanding the current broadband noise prediction method and its limitations. This, in turn, has influenced the development of the broadband noise prediction module in the ANOPP2 [5] noise prediction suite. While broadband noise predictions in this paper are presented using a semiempirical tool called Broadband Acoustic Rotor Codes (BARC) [6], the self-noise broadband prediction method is currently available in the ANOPP2 Self Noise Internal Functional Module (ASNIFM).

This paper will describe the technical approach of this study by presenting the rotor design method, the process used to manufacture the blades, the experiment and facility setup, and finally the low-fidelity noise prediction tools. Following this, experimental and predicted results are presented. These results will include performance measurements and processed acoustic data obtained in the hover chamber tests. In addition to this, experiments will be compared to tonal and broadband noise predictions. Limitations of the low-fidelity prediction methodology will be identified, followed by concluding remarks and possible future work for research on the ideally twisted rotor.

II. Technical Approach

A. Rotor Design

The rotor used in this study was designed using blade element momentum theory (BEMT) with an ideal twist distribution. This method, described in Ref. [7], defines a rotor experiencing uniform inflow and minimum induced power in hover. An ideally twisted rotor with a constant chord is defined by the following blade pitch distribution:

$$\Theta(r/R) = \frac{\Theta_{\text{tip}}}{r/R}, \tag{1}$$

and the local angle of attack and inflow angles are defined as:

$$\alpha(r/R) = \frac{\alpha_{\text{tip}}}{r/R}, \tag{2}$$

$$\phi(r/R) = \Theta(r/R) - \alpha(r/R). \tag{3}$$

The rotor consisted of four blades and was sized to a radius of R = 0.1588 m. The rotor was designed to generate 11.12 N (2.5 lbs.) of thrust at a rotational speed of Ω_c = 5500 RPM. The resulting thrust coefficient was C_T = 0.0137, with a tip Mach number of M_{tip} = 0.27. The distribution of Θ, α and ϕ along the span can be seen in Fig. 1. The nominal tip angles were a blade tip pitch of Θ_{tip} = 6.9 degrees, induced angle of ϕ_{tip} = 4.7 degrees, and angle of attack of α_{tip} = 2.1 degrees. The design parameters and conditions for the rotor in this study are summarized in Table 1.

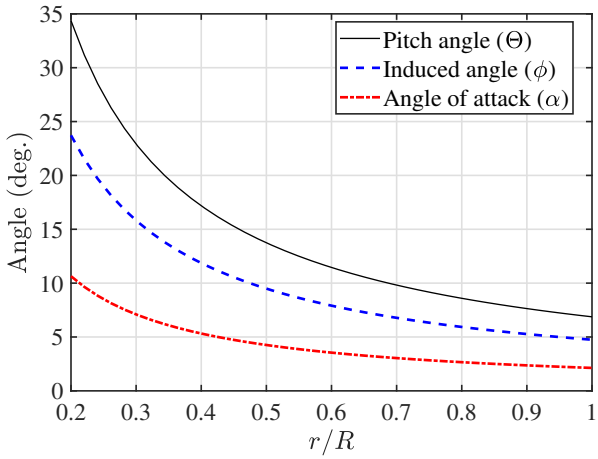

Fig. 1 Spanwise angle distributions for designed ideally twisted rotor.

Table 1 Ideally twisted rotor design parameters.

	Parameter	Value
Geometry	R (m)	0.1588
	c/R	0.20
	Θ_{tip} (°)	6.9
	N_b	4
	σ	0.255
Operating Condition	C_T	0.0137
	M_{tip}	0.27
	Ω_c (RPM)	5500

B. Blade Manufacturing

Various blade sets were manufactured and tested in the hover chamber, but this paper will focus on three sets:

- A smooth surface blade set printed in-house
- A smooth surface set printed by a contractor
- A rough surface blade set printed by a contractor

(a) Blade printing iterations

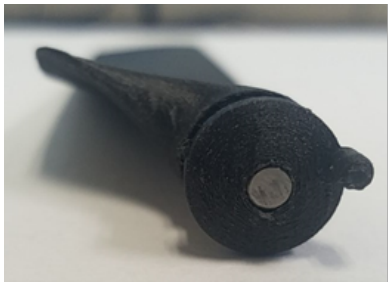

(b) Blade root design with aluminum spar

Fig. 2 Rotor blade manufacturing.

Preliminary rotor blades were printed in-house because several printing iterations were expected due to the tall and thin structure of the rotor blades. The first set of blades tested in this study were printed out of Onyx material [8], a micro carbon fiber filled nylon plastic. The blades were manufactured at the NASA Langley Larkworks MakerSpace using a Markforged X7 3D printer [9]. This printer has a build volume of 330 mm x 270 mm x 200 mm, and a minimum possible layer height of 50 μm. Different layers of plastic were printed in the radial direction to achieve acceptable surface finish without the need for post-processing, thereby mitigating potential for unbalanced blades. The blades were positioned such that they stood from the leading edge throughout the printing process. This layering technique resulted in a smooth airfoil definition in the chordwise direction. The blades were found to be challenging to print due to a combination of the blade orientation during layering as well as the fact that only one blade could be printed at a time. As Fig. 2(a) shows, the blades were printed with mixed success. However, the blades that did print successfully were of excellent overall build quality and surface finish.

In order to improve the stiffness of the blade, an aluminum ejector pin was inserted spanwise into the blade, to act as a spar, as shown in Fig. 2(b). The measured radius of the printed blade was 1.5% greater than the radius of the designed blade (0.1588 m). This may be due to thermal expansion occurring in the printing process. The mass of the blades averaged 17.781 grams, with 0.3% maximum mass difference. The in-house blades, pictured in Fig. 3(a), provided initial measurements in the first phase of testing, which provided a basis for early predictions and computations [3], but it became clear that a more rigid, stronger and geometrically accurate set of blades would be necessary. This is discussed further in Section III.A.

In a second phase of the testing campaign, the printing of several sets of blades was contracted out to Protolabs [10]. A blade set was manufactured via stereolithography (SLA). These blades were made of an "ABS-like" [11] material; this material was selected for its high tensile strength and lower elongation at break properties. The blades printed by this process had a radius within 0.1% of the 0.1588 m designed radius. The mass of the blades averaged 17.043 grams, with 0.4% maximum mass difference. A photo of one of these blades can be seen in Fig. 3(b), and these blades will be referred to as "smooth" blades in this paper, as their surface has a homogeneously smooth texture. Another blade set was manufactured via selective laser sintering (SLS). These blades were made of a material called PA-12, which is a 25% mineral-filled nylon material [12]. They are stiff blades, and the surface finish of these blades has a homogeneous and "grainy" texture. These blades had a radius within 0.1% of the 0.1588 m designed radius. The mass of the blades averaged 16.026 grams, with 0.8% maximum mass difference. A photo of one of these blades can be seen in Fig. 3(c), and due to their surface texture, they will be referred to as "rough" blades in this paper.

(a) In-house Markforged Onyx Blades

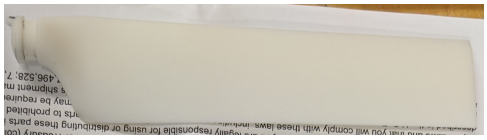

(b) Protolabs SLA ABS-like Smooth Blades

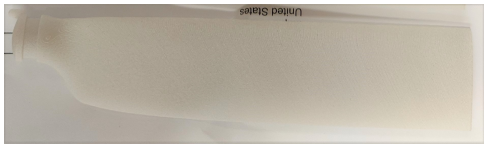

(c) Protolabs SLS PA-12 Rough Blades

Fig. 3 Rotor blade iterations.

All the blade roots were designed to mate with a COTS hub made by varioPROP [13], which is a small-scale ground adjustable variable pitch propeller hub (see Fig. 4). Using this hub it was possible to manually adjust the pitch of all 4 blades simultaneously.

Fig. 4 Photos of COTS varioPROP hub.

C. Experimental Setup

The experiments were conducted in the Small Hover Anechoic Chamber (SHAC), a facility at the NASA Langley Research Center. Photos of the setup are shown in Fig. 5. The SHAC is acoustically treated down to 250 Hz and has working dimensions of 3.87 m x 2.56 m x 3.26 m. This facility was found in recent studies to be suitable for measuring the aerodynamic loads and acoustics of small rotors in static conditions when proper precautions are taken to address and mitigate the effects of flow recirculation [1, 14]. Two mesh screens of open areas 72% and 51% were placed five and nine rotor radii, respectively, downstream from the rotor to reduce recirculation effects, as seen in Fig. 5(c). The effect of this recirculation mitigation technique will be discussed in Section III.B. A Brüel & Kjær (B&K) LAN-XI data acquisition (DAQ) and BK Connect software system were used for data acquisition. Six B&K Type 4939 free-field microphones are located in the upper corner of the SHAC, and span a range of +43.5° above the plane of the rotor to −43.1° below the plane of the rotor. These microphones are located at a minimum of 12 rotor radii away from the rotor, which is in the acoustic far-field. A laser sensor tachometer located directly below the rotor was used to monitor the rotation rate of the rotor, and a 6-component AI-IA mini40 multiaxis load cell was used to measure the aerodynamic forces. The rotor was powered using a Scorpion 4020 DC brushless motor and a Castle Creations Edge 50 electronic speed controller.

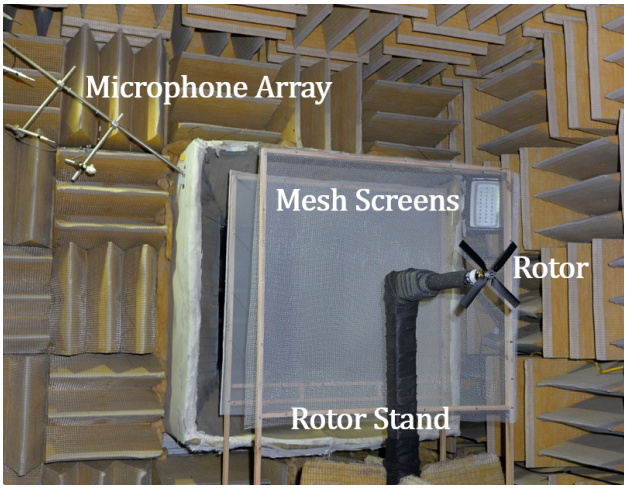

(a) Testing setup in SHAC facility

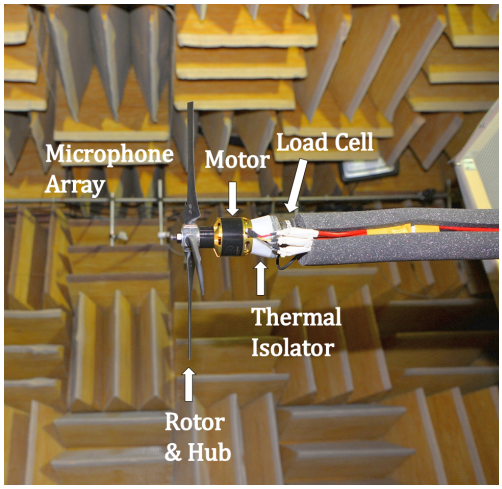

(b) Mounted rotor, motor and load cell

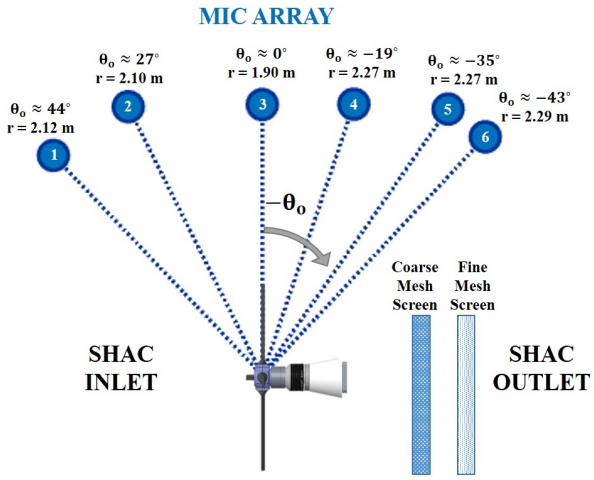

(c) Acoustic measurement layout (not to scale)

Fig. 5 SHAC facility and acoustic measurement configuration.

During testing, two parameters were varied: rotor rotation rate (Ω) and rotor collective (A_0). A sweep of rotor rotation rates was first acquired at the designed blade tip pitch of $\Theta_{tip} = 6.9°$ to establish the target design operating condition. Following this, rotor rotation sweeps were performed at two additional target pitches of $\Theta_{tip} = 3.9°$ and $9.9°$. To set the tip pitch of the blades, the root pitch was adjusted with a set screw in the varioPROP hub while monitoring the pitch at the tip with an RC Logger digital pitch gauge. This method was found to be precise within $A_0 = \pm 0.4°$. A summary of the testing condition targets is provided in Table 2. It should be noted that the tip pitches listed in the table are targets, but heretofore the rounded $\Theta_{tip} = 4°$, $7°$ and $10°$ values will be used when describing the experiment. Only the Protolabs smooth blades were tested at all rotation rate and tip pitch conditions.

Table 2 Experiment target conditions.

Parameter Sweep	Ω (RPM)	Θ_{tip} (°)
Rotation Rate (Ω)	3000⇒5800* †	6.9
Rotor Collective (A_0)	5500*	3.9, 6.9, 9.9

*Values are approximate.
†Tested in approximate increments of 500 RPM.

D. Low-Fidelity Prediction Tools

Several low-fidelity rotor performance and acoustic prediction tools are utilized in this study. The first two are part of the NASA Aircraft NOise Prediction Program (ANOPP), and are called the Propeller Analysis System (PAS) [15] and the Rotorcraft System Noise Prediction System (ROTONET) [16]. These codes utilize BEMT to predict the aerodynamic loads on respective propellers and rotors.

PAS is utilized to predict the tonal noise characteristics of the ideally twisted rotor due to it utilizing an acoustic solver that accounts for the full pressure distribution on the blade surface, whereas ROTONET utilizes a compact chord assumption. An inflow velocity is required as an input into PAS, and therefore, predicted inflow characteristics cannot truly represent a hover condition. PAS has been found to produce reasonably accurate predictions of a hover condition with a modest freestream velocity condition setting [2]. In this study, however, ROTONET is utilized to compute the inflow characteristics for the rotor in a hover condition, as it can model this condition with better accuracy than PAS. The ROTONET performance module assumes a fully articulated rotor with rigid blades and a simple uniform inflow model [17].

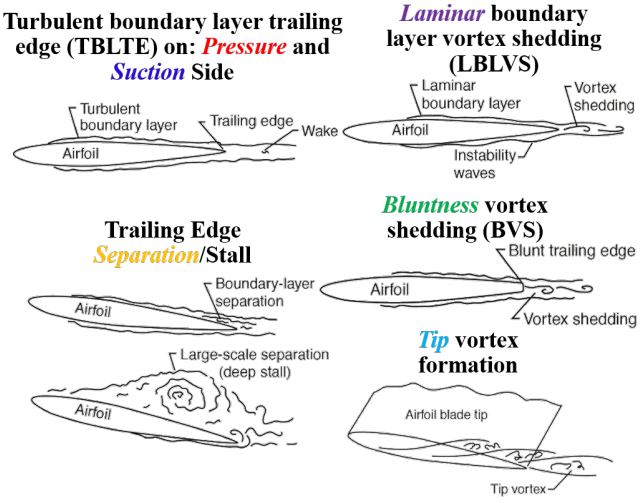

Fig. 6 Self-noise mechanisms predicted by BARC. For more information on these noise sources, please see Refs. [2, 4, 6, 18].

Broadband rotor self-noise predictions are currently performed using the Broadband Acoustic Rotor Codes (BARC) suite [2, 4, 6, 18]. This suite incorporates the semiempirical airfoil self-noise prediction routines of Ref. [18] into a rotating reference frame, given the appropriate aerodynamic conditions of discrete blade elements. ROTONET uses rotor definitions and flight conditions such as thrust, rotor angle, rotor speed, advance ratio and trim conditions as inputs in order to calculate inflow conditions for BARC. The self-noise prediction method uses empirical boundary layer data obtained from untripped and physically tripped flow over an NACA0012 airfoil to define the boundary layer parameters. Thus, BARC also requires a "tripped" or "untripped" boundary layer flag as an input. The self-noise mechanisms that will be predicted and discussed in this paper are displayed in Fig. 6.

Additional broadband noise sources, like blade wake interaction (BWI) [19] and turbulence ingestion noise (TIN) [20], cannot be modeled with these low-fidelity tools. Noise predictions using a lattice-Boltzmann method solver are presented in a companion paper (Ref. [3]), which addresses these noise sources.

III. Results

A. Performance Measurements

As described in Section II.C, a sweep of rotation rate conditions was performed for the nominal design blade pitch of $\Theta_{tip} = 7°$. At this design blade pitch condition, a full rotation sweep was tested for the in-house blades and smooth blades. For the rough Protolabs blades, only three rotation rates were tested at the design blade tip pitch condition. For the smooth Protolabs blades, the collective was adjusted such that the blade pitch at the tip was ±3° from the baseline condition. The smooth blades were only run up to a rotation rate of 5500 RPM for the $\Theta_{tip} = 10°$ case as a precaution due to greater expected loads. The rotor coefficient of thrust is plotted against the mechanical rotation rate in Fig. 7 for the various blades at the described performance conditions. The thrust coefficient is expected to remain constant if the only parameter being varied is the rotation rate. The in-house blades showed high variance in thrust coefficient with varying rotation rate, indicating blade deflection occurring at the nonbaseline conditions. The smooth Protolabs blades did have a more constant thrust coefficient, though it still varied (see slope values in the legend of Fig. 7). There are not enough data points for a reliable curve fit of the rough Protolabs blades.

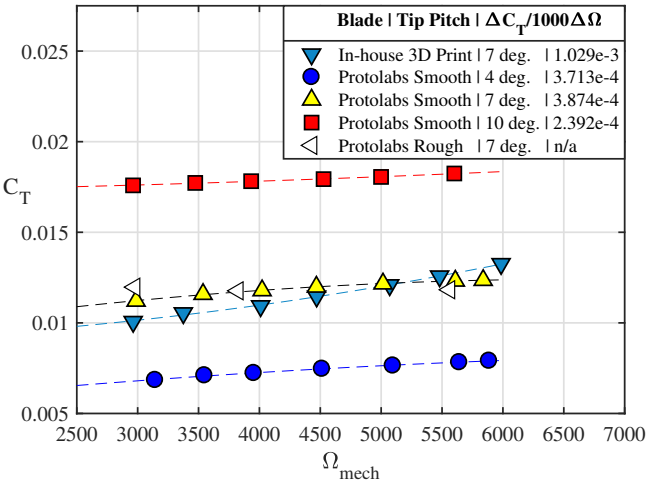

Fig. 7 Thrust coefficient plotted against rotation rate for four rotation rate sweeps. First-order curve fits were applied to data (see legend for slopes).

Dimensional thrust is plotted against rotation rate (corrected for standard day conditions) in Fig. 8(a) for the smooth Protolabs blades. Similarly, dimensional torque is plotted against rotation rate in Fig. 8(b). A second-order polynomial curve fit was applied to each set of rotation sweep data for both thrust and torque profiles. For the baseline tip pitch case ($\Theta_{tip} = 7°$), the measured thrust was 9.26% lower than that of the designed target thrust of 11.12 N. There are two possible explanations for this underperformance. First, the margin of error in setting the blade tip pitch may have been sufficient enough that the blade was pitched less than the measured 6.9 degrees. Second, the BEMT design methodology did not take into account tip loss effects.

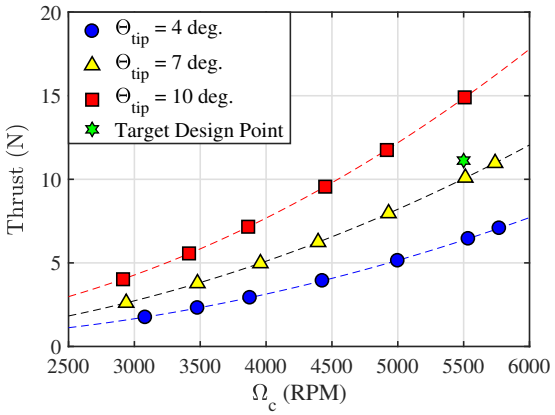

(a) Thrust plotted against rotation rate.

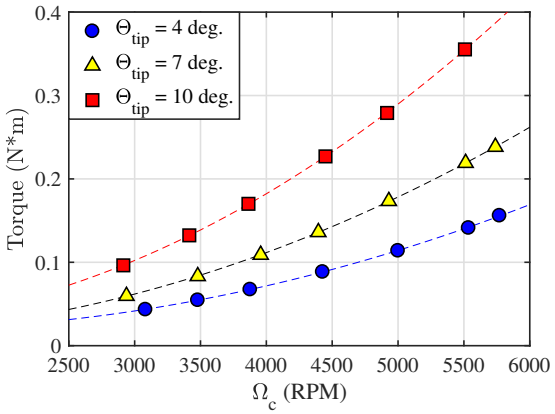

(b) Torque plotted against rotation rate.

Fig. 8 Thrust and torque are plotted against corrected rotation rate for the Protolabs smooth blade set tests. A second-order fit is applied to each rotation rate sweep (dashed lines).

B. Acoustic Measurements and Processing

In addition to performance data, microphone data were acquired by the six microphones described in Section II.C. The sampling rate for each data run was 130 kHz. Each run started with the motor ramping up to the desired target rotation rate. The acquisition time varied from run to run, but averaged approximately 10 seconds. This duration of time was chosen because it was expected to be within the onset of recirculation in the chamber. The effects of recirculation, which have been discussed in Refs. [1] and [14], are present in this study. It is important to note that the recirculation mitigation technique, specifically the mesh size, is unique to the facility and rotor in question. Initial tests without a mesh screen produced less than one second of uncontaminated data at a baseline condition, but with the current set up, the duration of uncontaminated data is at least 2 seconds long. Figure 9 shows the effects of recirculation on the fourth, eighth, twelfth and sixteenth shaft harmonics (373 Hz, 747 Hz, 1120 Hz, 1494 Hz, etc.), which correspond to the harmonics of the blade passage frequency for a four bladed rotor. The fundamental shaft harmonic is defined by the rotation rate of a single blade, $\Omega/60$, and the blade passage frequency is defined by the fundamental shaft harmonic multiplied by the number of blades.

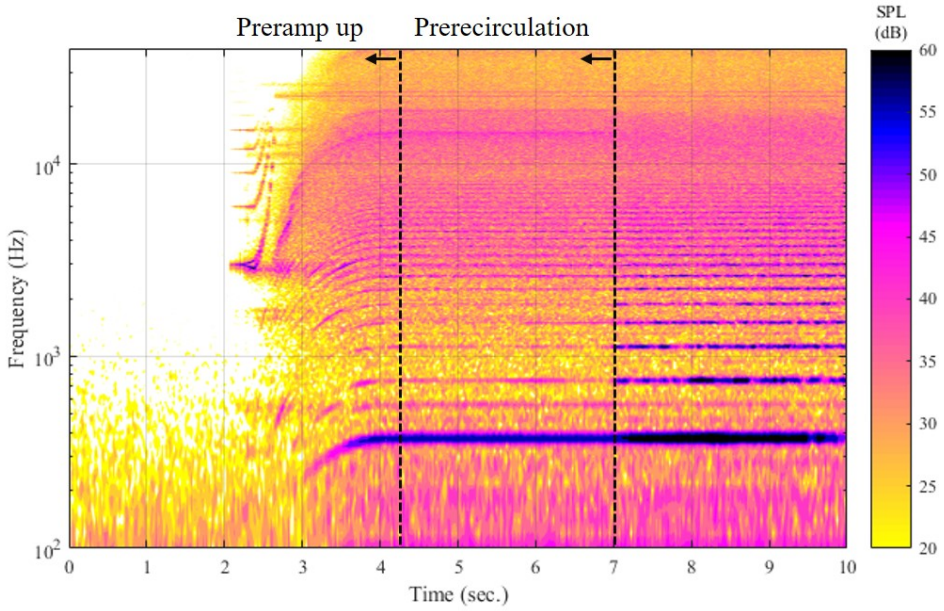

(a) Acoustic Spectogram for microphone 5

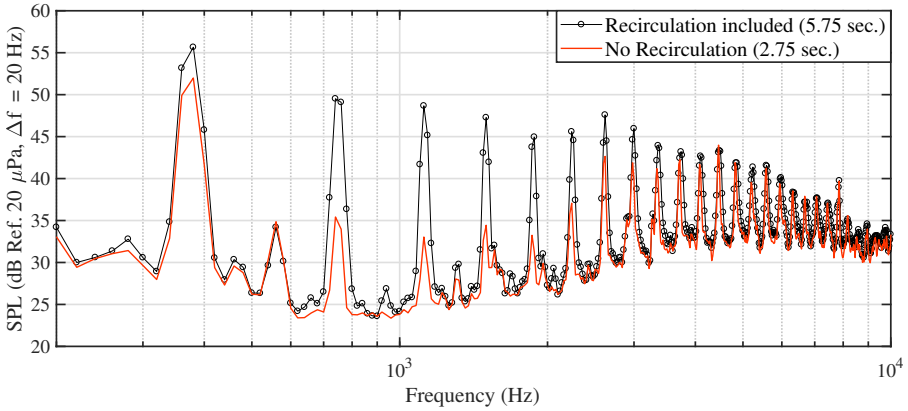

(b) Acoustic Spectra for microphone 5

Fig. 9 Recirculation effects on shaft harmonics of baseline case (Note: case shown represents Ω_c = 5510 RPM, Θ_{tip} = 7 deg.).

The following steps were taken to extract the stochastic, broadband content from the raw data. First, the narrowband acoustic spectra were computed by using a fast Fourier Transform (FFT) of raw data treated as random data sets. This raw spectrum is plotted in Fig. 10(a). Second, to separate the periodic and random components, the mean rotor revolution time history was computed. This was then subtracted from the time record to retain random noise components. An FFT was used to compute the periodic and broadband spectra from these mean and residual time series, and both spectra are plotted in Fig. 10(b). For greater detail on these two data processing technique please see Ref. [2, 21]. Finally, remaining peaks left in the residual signal were removed to more clearly see the broadband component. This "peak-removed" spectrum can be seen in black in Fig. 10(c). This final resulting spectrum is used for comparison with predictions; though it should be noted that the peak removal technique may not always be entirely effective, as it sometimes removes broadband noise content. When looking at an individual case, the broadband noise spectrum will be presented with peaks included. These spectra will be denoted with the subscript "bb". However, to make trends in rotation rate clearer, spectral plots with multiple rotation rate conditions will be presented with peaks removed, as they still represent the trends in broadband noise. These spectra will be denoted with the subscript "bb,pr".

The acoustic time series was also filtered to retain the harmonics of the BPF, using a second-order Butterworth narrow band-pass filter with a ± 20 Hz band around the BPF. The amplitude of the BPF was computed by calculating the RMS of the ensemble-averaged time history. For more details on this technique please see Refs. [2, 21],

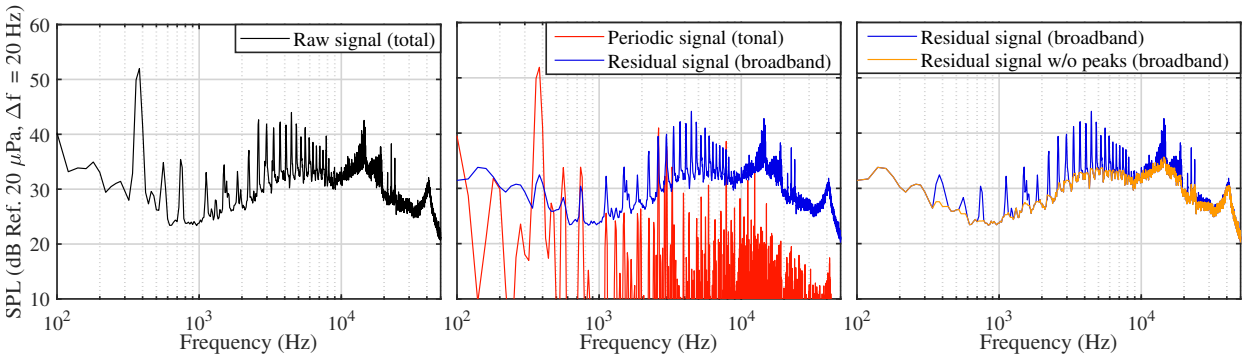

(a) Step 1 (b) Step 2 (c) Step 3

Fig. 10 Processing steps for isolation of periodic and broadband noise contributions.

C. Noise Characteristics and Trends

For the purposes of this paper, presented acoustic spectra will correspond to an observer located −35° below the plane of the rotor (microphone 5). This out-of-plane location is where broadband noise sources have the most prominent amplitudes [22]. Acoustic results will be presented for the Protolabs smooth and rough blades, and exclude those of the in-house blades.

1. Spectral Content

To examine the relative acoustic contributions of the broadband noise sources to the overall noise, a spectral interrogation of the baseline case ($\Theta_{tip} = 7°, \Omega_c = 5510$ RPM) is presented in Fig. 11. The narrowband total raw spectrum, residual broadband noise content and residual broadband noise with peaks removed are plotted. Fig. 11 also presents the background noise of the facility, as well as an equivalent motor only run. The fundamental blade passage frequency tone is clearly visible at 373 Hz. The broadband noise extraction removes the tonal content of the first and second BPF tone, but there is residual tonal content remaining at the third BPF and at higher harmonics of the BPF. Broadband noise dominates at frequencies higher than 1 kHz, but the residual broadband noise has a considerable amount of remaining tonal content, especially at frequencies between 1 kHz $\leq$ f $\leq$ 20 kHz. The motor produces tones at frequencies between 20 kHz $\leq$ f $\leq$ 25 kHz, which show up in the rotor noise signal, though minimally. The spike at 55 kHz in the facility noise spectrum is a result of limitations in the data acquisition of the microphone signal, but rotor noise levels for this case are high enough to be minimally affected by this.

Another spectral interrogation is performed on the lowest rotation rate case ($\Theta_{tip} = 7°, \Omega_c = 2938$ RPM) in Fig. 12. Due to the low rotation rate, the blade passage frequency is too low in frequency and amplitude to be visible in these data; therefore, rotor broadband noise is completely dominant for this condition. As with the baseline case, tonal

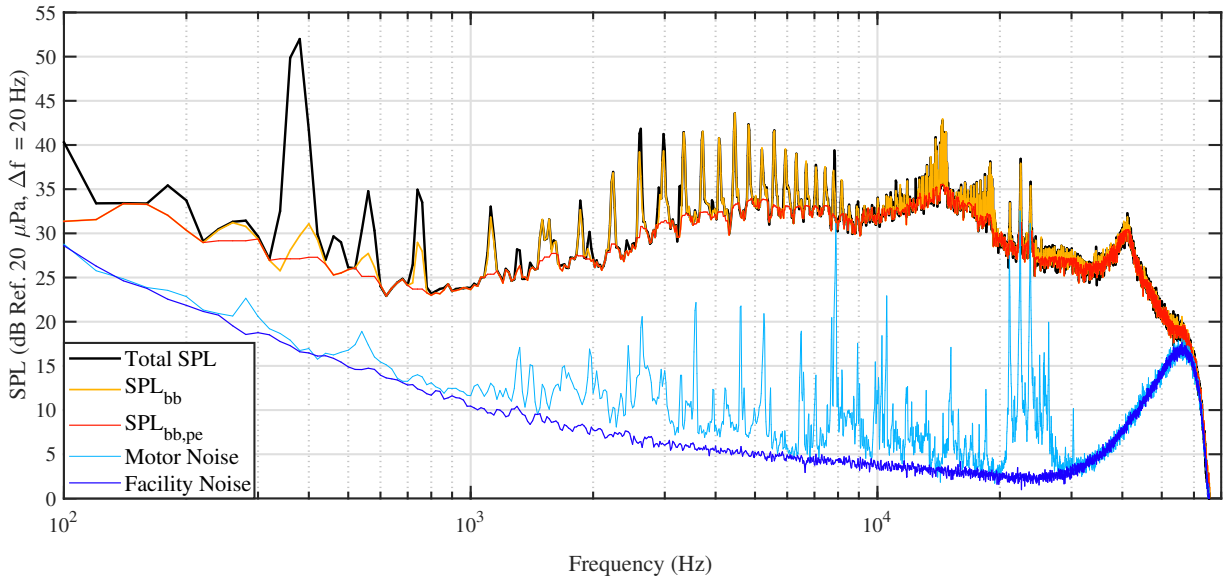

Fig. 11 Experimental noise spectra for the design tip pitch, baseline rotation rate condition (Θ_{tip} = 7°, Ω_c = 5510 RPM).

content remains in the residual broadband signal. When peak removal is employed for these data, the amplitude of the broadband noise shelf is reduced, a limitation that starts to become visible at around 3 kHz. For this condition, noise above 30 kHz is not a physical mechanism, but the result of limitations in the data acquisition of the microphone signal. The motor noise has a significant effect on the acoustic spectrum at frequencies between 20 kHz ≤ f ≤ 25 kHz. Motor noise remains at these frequencies independent of operating condition.

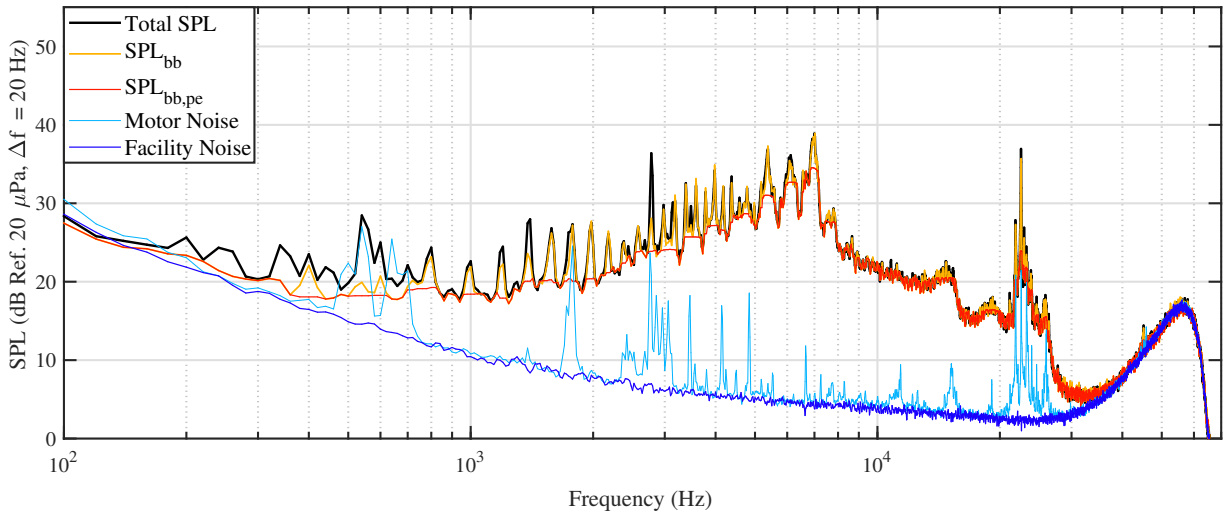

Fig. 12 Experimental noise spectra for the design tip pitch, low rotation rate condition (Θ_{tip} = 7°, Ω_c = 2938 RPM).

The unweighted overall sound pressure levels (OASPLs) at all observers are presented in Fig. 13(a) for the high rotation rate case and Fig. 13(b) for the low rotation rate case. The test cases with tip pitch conditions of 4° and 10° are included in these directivity plots along with the baseline tip pitch condition of 7°. For the high rotation rate cases ($\Omega_c \approx$ 5500 RPM), the spectra were integrated over the frequency range of 1 kHz to 55 kHz; for the low rotation rate

cases ($\Omega_c \approx 3000$ RPM), the spectra were integrated over the frequency range of 1 kHz to 30 kHz. The reason for the tighter range for the low rotation rate case is to avoid the background noise contribution discussed previously. A notable difference between Figs. 13(a) and 13(b) is that the broadband noise contribution increases with pitch for the 5500 RPM cases, but decreases with pitch for the 3000 RPM cases. A further analysis into these pitch trends is warranted and will be discussed in the following section.

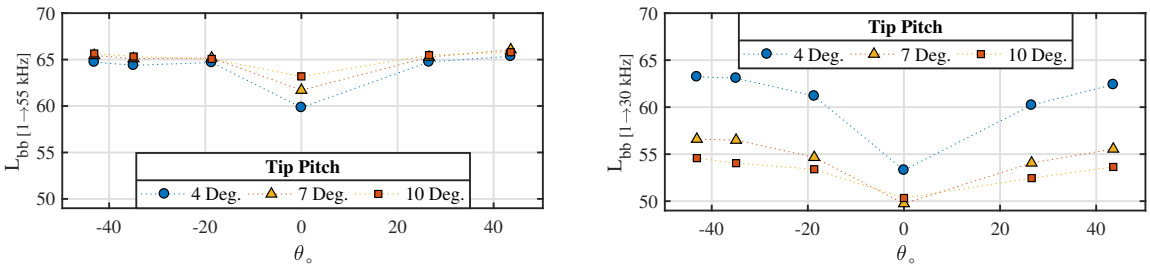

(a) $\Omega_c \approx 5500$ RPM

(b) $\Omega_c \approx 3000$ RPM

Fig. 13 Broadband noise sound pressure levels (L_{bb}) for all 6 microphone locations.

2. Noise Trends

By changing the tip angles but maintaining the same rotation rates, the loading on the blades is changed while maintaining the same tip speed, as presented in Section III.A. Figure 14 shows the spectra for the different blade pitch conditions of $\Theta_{tip} = 4°$, 7° and 10°, at the baseline tip speed. A few observations can be made when comparing the spectra of the three tip pitch conditions. First, between the frequencies of 12 kHz $\leq$ f $\leq$ 25 kHz, broadband noise levels seem to decrease with increasing tip pitch. The spectral peaks between the frequencies of 13 kHz $\leq$ f $\leq$ 19 kHz are indicative of laminar boundary layer vortex shedding (LBLVS), and are present in both baseline and low tip pitch cases. Finally, at the highest frequencies between 35 kHz $\leq$ f $\leq$ 55 kHz , a high frequency noise source is present at the high and mid tip pitch conditions, and not present for the low tip pitch condition of $\Theta_{tip} = 4°$. The high frequency noise source was initially believed to be bluntness vortex shedding (BVS) noise; however, this noise source is absent for the $\Theta_{tip} = 4°$ condition, and it experiences a large amplitude shift with blade tip pitch.

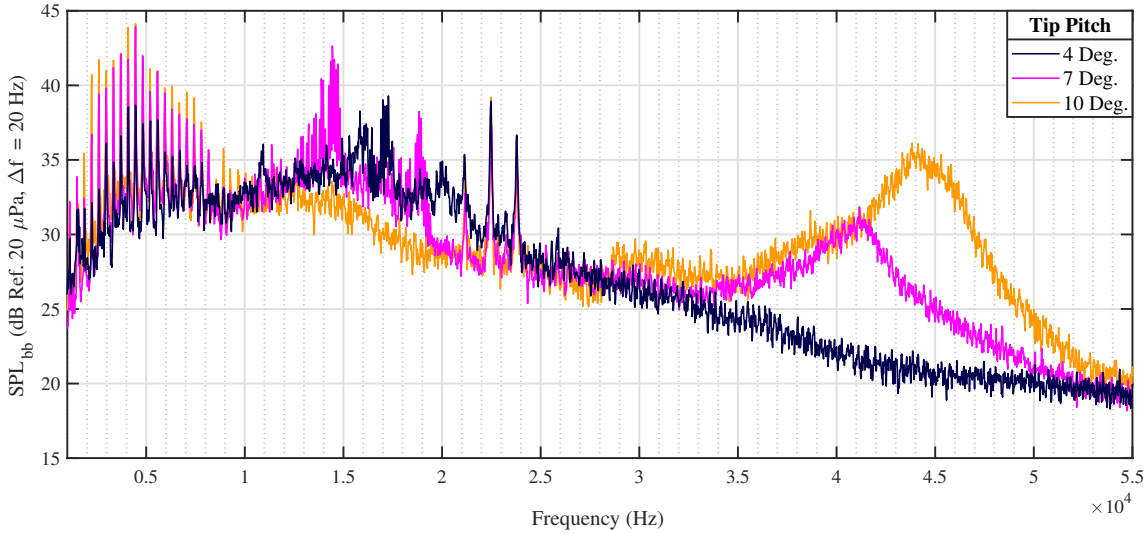

Fig. 14 Varying tip pitch for the baseline rotation rate cases ($\Omega_c \approx 5500$ RPM).

The spectral content trends with blade tip pitch are present in all out of plane observers. Figure 15 shows OASPL plots for the three tip pitch conditions at approximately 5500 RPM, integrated over several frequency ranges. The integration ranges are: 1 kHz ≤ f ≤ 10 kHz, 10 kHz ≤ f ≤ 25 kHz, and 25 kHz ≤ f ≤ 55 kHz. The earlier Fig. 13(a), presented OASPL over the entire frequency range where broadband noise is present (1 kHz ≤ f ≤ 55 kHz); but by separating out the frequency ranges into a low, mid and high frequency ranges, it is apparent that broadband noise does not uniformly increase with blade tip pitch. Both the spectra including the peaks and without the peaks are shown, as they increase overall levels at the low and mid frequency ranges. The peaks in the residual broadband noise signal have a more significant impact on the mid frequency range on the low and mid tip pitch conditions.

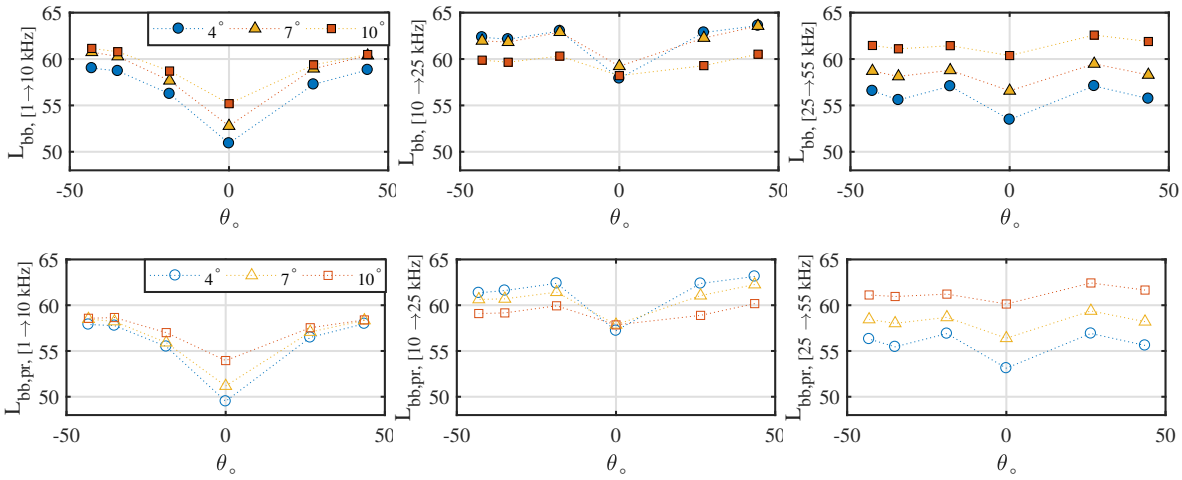

Fig. 15 Integrated sound pressure levels for residual noise at $\Omega_c \approx 5500$ RPM. Noise was integrated over three frequency ranges. Colored symbols use residual broadband signal with peaks (L_{bb}), while clear symbols use residual broadband signal with peaks removed ($L_{bb,pr}$).

It is also important to analyze the spectra of the different blade pitch conditions of Θ_{tip} = 4°, 7° and 10°, at the low tip speed, which is presented in Fig. 16. As was shown earlier for the baseline rotation rate cases, there is a noticeable amount of broadband noise at frequencies ranging from 3 kHz ≤ f ≤ 10 kHz, which seems to increase in amplitude, and reduce in frequency range with decreasing blade tip pitch. The low rotational cases are where LBLVS is believed to be most prominent, due to the lower local Reynolds numbers experienced by the blade. The amplitude of this noise source decreases with increasing blade tip pitch, and the frequency over which it is spread increases with blade tip pitch setting. There is a high frequency broadband noise shelf, that increases in frequency with tip pitch angle, which ends at approximately 13, 14 and 17 kHz for the low, mid and high tip pitch conditions, respectively. This noise source is believed to be due to bluntness vortex shedding.

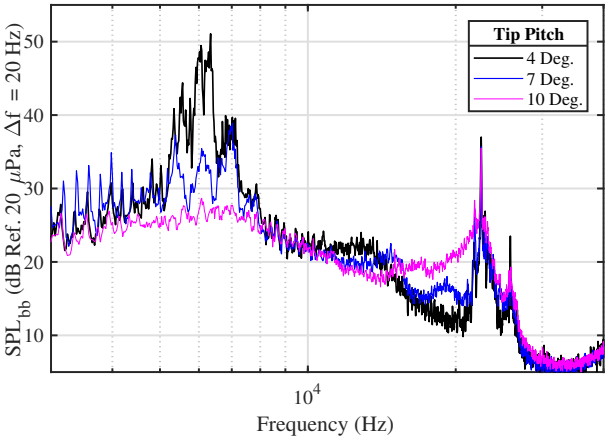

Fig. 16 Varying tip pitch for the low rotation rate cases ($\Omega_c \approx 3000$ RPM).

After examining effects of varying the blade tip pitch on spectra for the high and low rotation rate cases, another analysis can be made on the effect of varying only rotation rate, in order to identify any transitional acoustic behavior between the high and low rotation rates. Figure 17 shows broadband noise for all six rotation rate cases at Θ_{tip} = 4°, 7° and 10°. To clearly see the differences in thrust conditions, the broadband noise is presented with peaks removed ($SPL_{bb,pr}$). As described earlier, the increase in high frequency content between 50 kHz ≤ f ≤ 60 kHz present in the lower RPM cases is not a physical mechanism, but the result of limitations in the data acquisition of the microphone signal. Additionally, motor noise located between 21 kHz ≤ f ≤ 26 kHz is present in the data for all testing conditions.

The noise at the frequencies below approximately 1 kHz is believed to be due to disturbances near the microphone. The following observations can be made when looking at these figures. First, all three tip pitch conditions exhibit transition-like behavior as rotation rate is increased. For instance, the mid frequency hump attributed to LBLVS at the 3082 RPM condition in Fig. 17(a), located at frequencies between 3 kHz $\leq$ f $\leq$ 9 kHz, increases in frequency range with rotation rate. It also reduces in relative contribution to the broadband noise spectra as rotation rate is increased. This effect is present in Figs. 17(b) and 17(c), though not as apparent. A second observation is at approximately 4500 RPM (corresponding to the 4395 RPM condition in Fig. 17(b) and the 4449 RPM condition in Fig. 17(c)), a transition occurs where lower frequency noise rises to amplitudes comparable to that of LBLVS. A third observation is the shelf attributed to BVS at 3082 RPM condition in Fig. 17(a), located at frequencies between 9 kHz $\leq$ f $\leq$ 15 kHz, is slightly increasing in frequency with rotation rate. To understand these trends with rotation rate, the experimental data must be looked at further with spectral scaling.

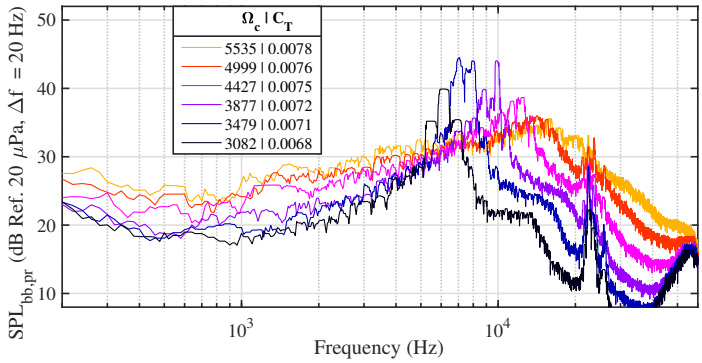

(a) Θ_{tip} = 4°

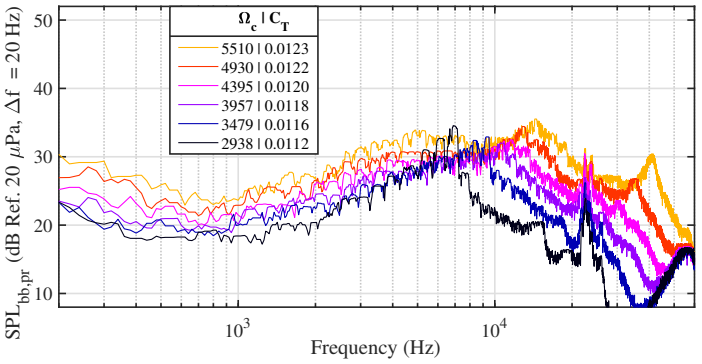

(b) Θ_{tip} = 7°

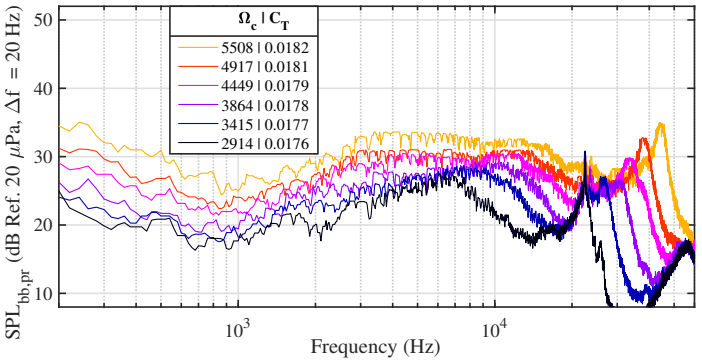

(c) Θ_{tip} = 10°

Fig. 17 Peak-removed broadband noise spectra for the set of rotation rate sweep experiments.

3. Spectral Scaling Behavior

The broadband self-noise sources are expected to scale in amplitude and frequency based on their respective scaling laws described in Ref. [18]. The spectral functions for each mechanism will not be explicitly defined here, but they are available in Refs. [6, 18].

Both dimensional and nondimensional trends of the broadband noise spectra are presented in Fig. 18 for the seven rotation rate cases. The peak-removed broadband spectra for the various thrust conditions are presented as one-third octave spectra ($SPL_{1/3}$) in Figs. 18(a), 18(c), and 18(e). The data were then nondimensionalized using the Strouhal number $St = f * H/U_{tip}$, with bluntness length, H, of 0.5 mm as the length scale, and tip Mach number, M_{tip}^5, of the highest rotation rate case for each blade tip pitch condition, as the velocity scale. The results of scaling can be seen in Figs. 18(b), 18(d), and 18(f). There are data at Strouhal numbers higher than 0.3 presented in Fig. 18 for completeness, which do not scale and should be disregarded as this is due to background noise. There are also some data contaminated with motor noise, which will not scale in frequency. This is most obvious in the low rotation rate cases, at the Strouhal number value of 0.24. While the high rotation rate cases have motor data that would correspond to the region of interest of the Strouhal number value of 0.1, the contribution of the motor to the overall rotor spectra is minimal at the high rotation rate cases (as explained in Section III.C.1).

This scaling scheme was chosen to attempt a midfidelity collapse of the data based on a single reference length and velocity scale. In reality, the different broadband mechanisms warrant different length and velocity parameters related to the boundary layer parameters. The spanwise variability of these conditions along the rotor blades in question, however, make this type of scaling difficult to perform. Additionally, the scaling parameters H and M_{tip}^5 are measured directly in the experiments, and do not require a boundary layer model to compute. Therefore, H and M_{tip}^5 were believed to be appropriate based on the trailing edge bluntness being commensurate with the boundary layer thicknesses and the fifth power of tip velocity representative of most self-noise scaling models used in Ref. [18]. This scaling is seen to collapse data for all conditions across Strouhal number ranges of $0.01 \leq St \leq 0.03$ and $0.1 \leq St \leq 0.2$, with considerable deviations between these ranges.

The Strouhal region of $0.01 \leq St \leq 0.03$ collapses nicely for all three blade tip conditions. The dimensional amplitudes of this region are the same with tip pitch conditions at the same rotation rate; however, when scaled it is apparent that the amplitude starts to shift upward with tip pitch condition. This region is believed to be TBLTE noise, due to its 5th power collapse.

Between approximately $0.05 \leq St \leq 0.1$, the spectra are seen to transition from a prominent peak to a modest hump as the tip Mach number is increased. As illustrated previously in Fig. 12, this behavior is most prominent for the $\Theta_{tip} = 4°$ tip pitch condition. Both the degradation and forward frequency shift of this spectral feature are believed to represent laminar to turbulent boundary layer development. Additionally, because scaling uses the bluntness length H as the length scale, it is expected for bluntness vortex shedding to occur in the Strouhal range of $0.1 \leq St \leq 0.15$ based on Ref. [18].

The deviation regions are at Strouhal numbers of $0.033 \leq St \leq 0.1$, $0.03 \leq St \leq 0.1$, $0.04 \leq St \leq 0.13$, for the $\Theta_{tip} = 4°$, $\Theta_{tip} = 7°$ and $\Theta_{tip} = 10°$ conditions, respectively. The spectra at the highest rotation rates collapse well in these regions, for instance, at rotation rates $5510 \geq \Omega_c \geq 4395$ RPM in Fig. 18(d). This collapse is even better in Fig. 18(f). Thus, it seems that whatever noise source is causing this deviation comes into transition at a certain rotation rate.

Without knowing the nominal values of the boundary layer properties, the expected behavior of these properties is described by the boundary layer model for an NACA0012 in Ref. [18]. As the tip pitch condition increases, so does the local angle of attack. For both a tripped and untripped airfoil, the boundary layer properties of the suction side of the airfoil are expected to increase, while the boundary layer properties of the pressure side of the airfoil are expected to decrease. LBLVS has an amplitude dependence on the pressure-side boundary layer thickness, δ_p, so it is expected to decrease in amplitude with tip pitch condition. For example, in Figs. 18(b), 18(d), and 18(f), the peaks at the Strouhal number ranges of $0.06 \leq St \leq 0.08$ reduce in amplitude with tip pitch condition. There is variance in rotation rate, but a good example comparison would be between the Ω_c = 4427, 4395 and 4449 RPM cases in the three figures.

Another parameter that drives LBLVS is tip speed, and, thus, the chord Reynolds number. As rotation rate is increased for a constant tip pitch condition, the local Reynolds number is increased, as is the local angle of attack. The angle of attack increase is minimal though, for a uniform inflow condition. The boundary layer properties of both the pressure and suction side of the airfoil would reduce with increased speed. More specifically, the pressure-side boundary layer thickness, δ_p, would generally decrease with tip speed, thus decreasing LBLVS noise. An exception is noted in Fig 18(b) for the Ω_c = 3479 RPM and 3082 RPM cases. In Ref. [18], it is explained that at zero degrees angle of attack, LBLVS cannot develop. So, the LBLVS noise is expected to increase until a certain angle of attack, then start to decrease. This could be what is happening here, a transition from the close to zero degrees angle of attack condition

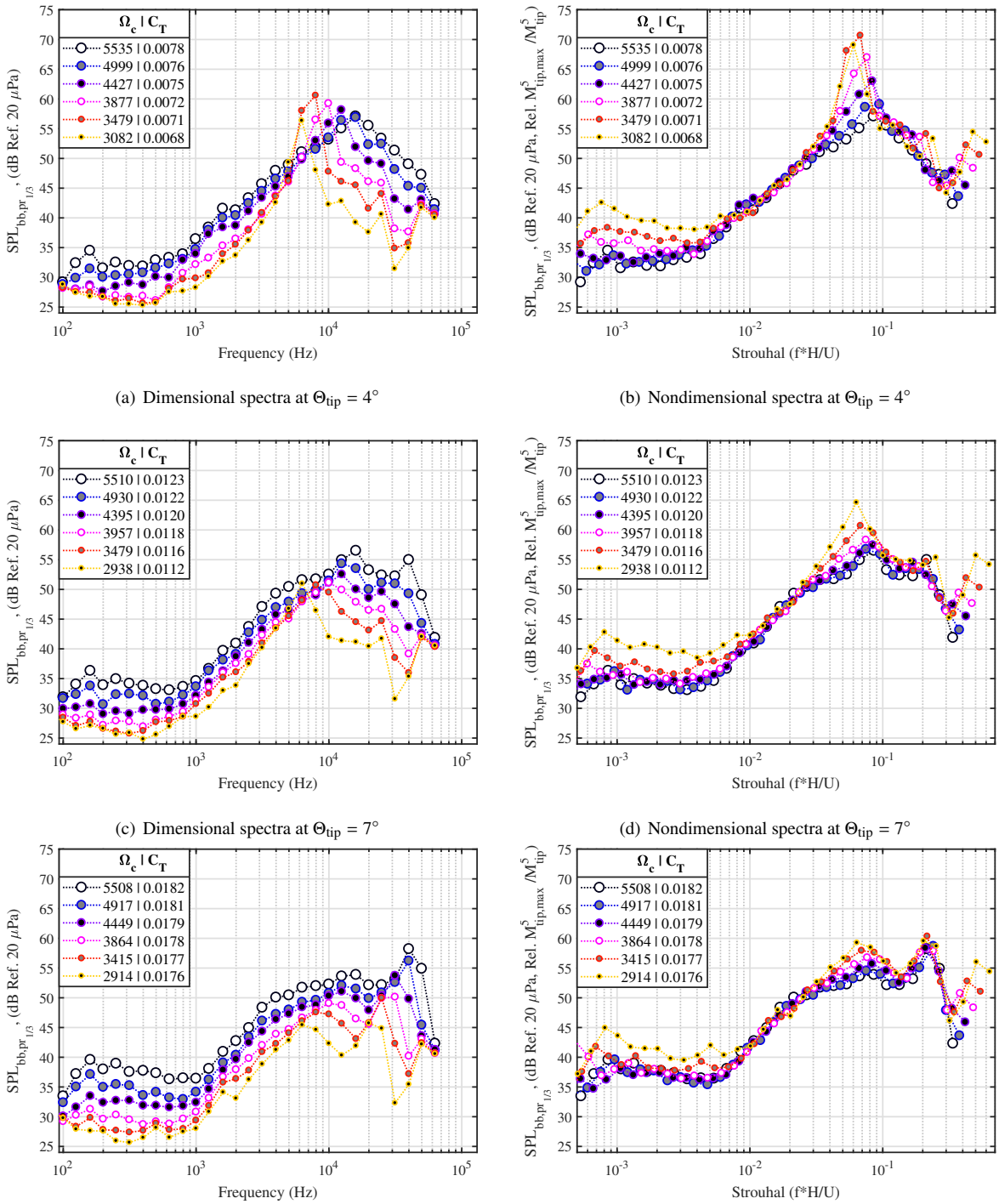

(a) Dimensional spectra at $\Theta_{tip} = 4°$

(b) Nondimensional spectra at $\Theta_{tip} = 4°$

(c) Dimensional spectra at $\Theta_{tip} = 7°$

(d) Nondimensional spectra at $\Theta_{tip} = 7°$

(e) Dimensional spectra at $\Theta_{tip} = 10°$

(f) Nondimensional spectra at $\Theta_{tip} = 10°$

Fig. 18 Processed broadband spectra for a range of rotation rate conditions.

that would exclude LBLVS from developing. The shape function used in Ref. [18] shows that as the chord Reynolds number increases, LBLVS "spreads out", over a larger frequency range as it reduces in amplitude. This behavior is most apparent in the low tip pitch conditions in Figs. 18(a) and 18(b).

4. Blade Comparison

As described in Section II.B, a smooth set of blades and a granular set of blades were tested in the SHAC. The two Protolabs blade sets were compared to each other in order to understand the effects of surface roughness on spectral content. The spectra for both set of blades at the baseline run condition at microphone 5 are compared in Fig. 19(a). At this condition, there are three noticeable differences. First, the noise source at 40 kHz is not present for rough blades. Second, the broadband peaks at frequencies in which LBLVS is thought to be present (14 and 19 kHz), are not present in the rough blade spectra. Lastly, there is significant additional noise for the rough blades at the low to mid frequency region of 1 kHz $\leq$ f $\leq$ 13 kHz, where TBLTE suction noise is thought to dominate. Another comparison is made for the low rotation rate condition, in Fig. 19(b). This comparison shows a greater difference in the LBLVS region. The lack of appearance of LBLVS for the rough blades provides evidence that the flow over the blades is likely turbulent.

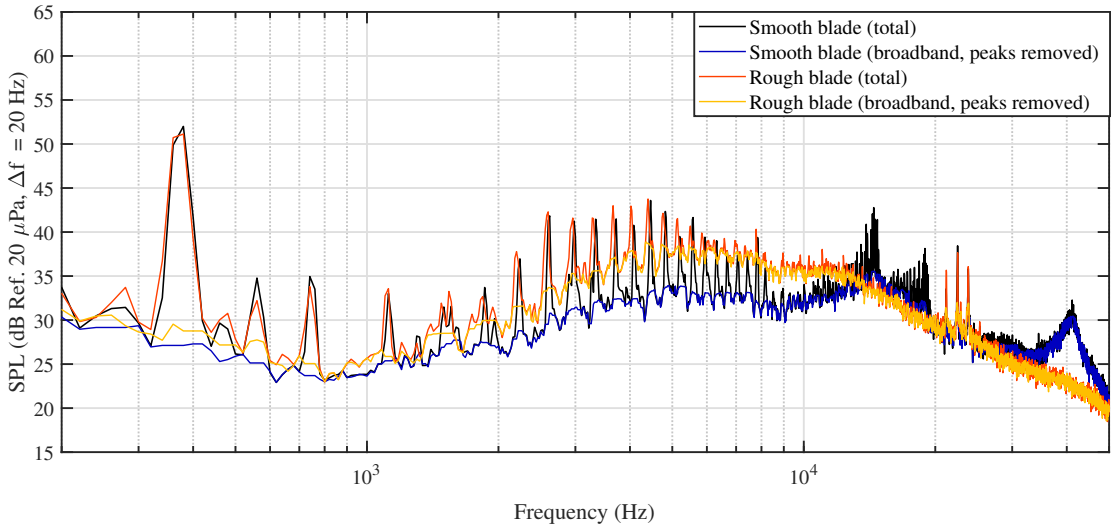

(a) $\Omega_c \approx 5500$ RPM

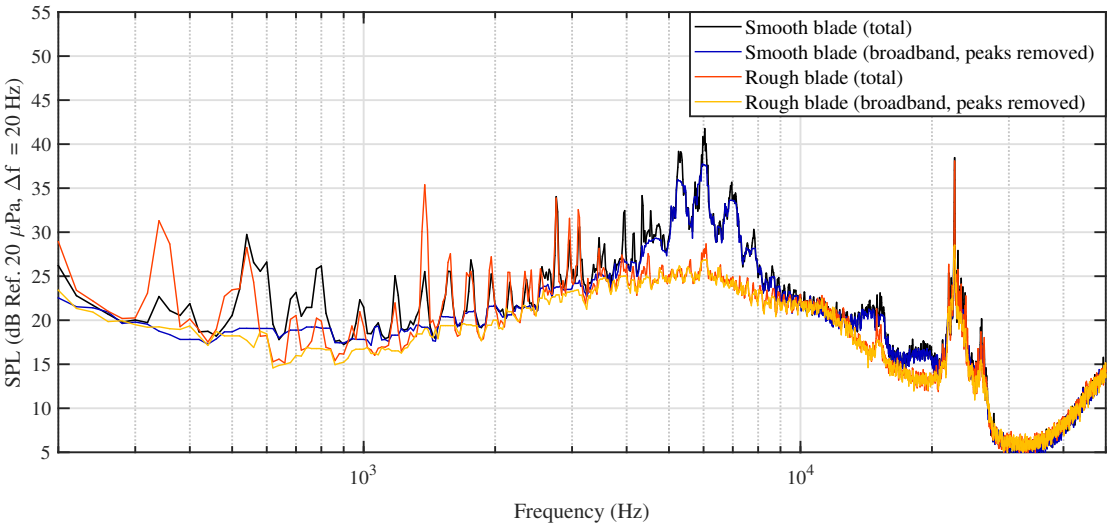

(b) $\Omega_c \approx 3000$ RPM

Fig. 19 Noise comparison between two blade sets at Θ_{tip} = 7 deg. with noticeably different surface roughness. All spectra are shown at microphone 5.

The noise spectra of the rough blades were nondimensionalized in a similar manner as was previously discussed for the smooth blades. For these cases, the data are plotted against Strouhal number using H = 0.8 mm as the length scale, as it is believed that the roughness could add a bit of thickness to the trailing edge. The effects of scaling the

data are seen in Fig. 20. The spectra are seen to not collapse as well across as many frequencies as the previously discussed smooth blades. This type of behavior is similar to that shown for TBLTE self-noise generation on the tripped airfoils studied in Ref. [18]. Reasonable spectral collapse is seen to occur, however, across the Strouhal number range of $0.1 \leq \mathrm{St} \leq 0.2$, which is the range at which BVS is expected to be exhibited.

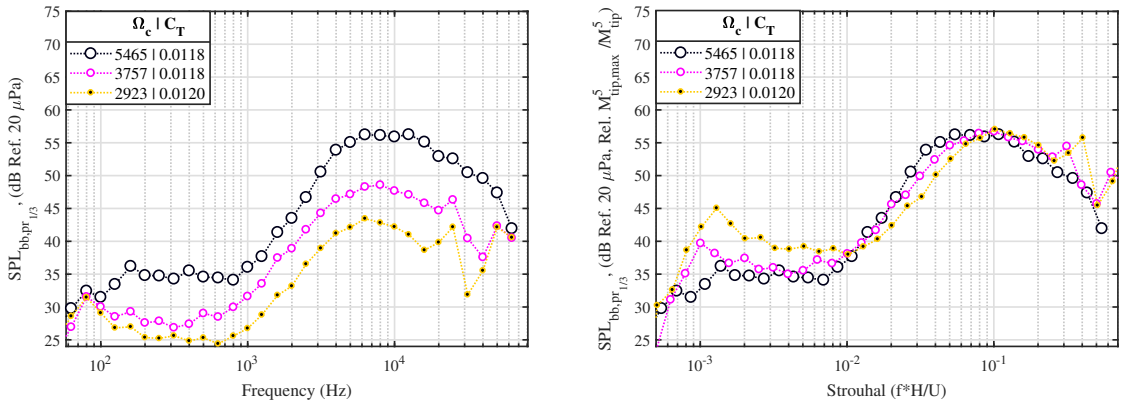

(a) Rough blade one-third octave spectra

(b) Scaled one-third octave spectra for rough blade

Fig. 20 All spectra are shown at microphone 5.

D. Tonal Noise Predictions

Figure 21 presents the fundamental BPF predictions and measurements for the smooth ideally twisted rotor for a range of directivities. PAS is used to perform a tonal noise prediction of the ideally twisted rotor at the target design operating condition. Fig. 21(a) shows the predicted fundamental BPF directivity for a range of observer elevation angles (see Fig. 5(c) for angle convention). Note that the data in this figure are normalized to a common radius of 1.90 m using spherical spreading. As Fig. 21(a) shows, the BPF directivity is seen to be thickness noise dominant across the entire range of computed observers. This is due to the relatively large rotor solidity due to the blade count, which reduces the aerodynamic loading per blade. As a result of this, it is expected that operating the rotor at different blade tip pitch conditions for a fixed rotation rate would yield similar noise levels. This is confirmed in Fig. 21(b), which shows commonality in directivity trends between the PAS predictions and SHAC measurements at the three different operating conditions. The experiments show a maximum difference in amplitudes between the lowest and highest blade pitch settings of 2.5 dB, which is very small compared to the considerable difference in thrust generated by the rotor at the different respective blade pitch settings (see Fig. 8(a)). These results provide further confidence in the low-fidelity blade design and prediction process.

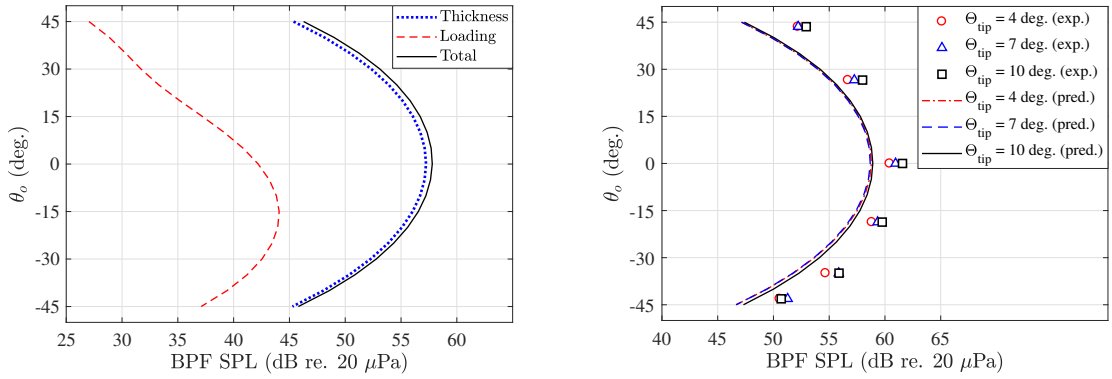

(a) PAS-predicted BPF directivity.

(b) BPF directivities for varying Θ_{tip}.

Fig. 21 Acoustic directivity predictions and measurements of rotor BPF: (a) noise contribution predictions using PAS at target operating condition ($\Theta_{\mathrm{tip}} = 7°, \Omega_c = 5510$ RPM), (b) comparison between PAS predictions and experimental SHAC measurements for different blade tip pitch conditions at $\Omega_c \approx 5500$ RPM.

E. Broadband Noise Predictions

Low-fidelity predictions of the broadband self-noise will be presented in this section. Using the low-fidelity tools, ROTONET and BARC, broadband noise was predicted to compare with experimental cases.

There are two options in matching the off-design conditions in ROTONET. First, there is the option to match the thrust coefficient to that of the experiment, resulting in a trimmed tip pitch prediction. Second, there is the option to match the tip pitch of the experiment, which would result in a constant thrust coefficient for all the cases. The second option was originally thought to work best; however, as described in Section III.A, the thrust coefficient is varying, implying twisting of the blade at off-design conditions. Additionally, the measured blade tip pitch could vary from the desired result by ± 0.4 degrees, so there is more confidence in predicting thrust than tip pitch angle. Thus, for ROTONET predictions, thrust was matched rather than the tip pitch angle.

The current prediction method is limited to one-third octave bands, but it is compared to the narrowband experiment with $\Delta f = 20$ Hz. This is done by dividing the energy from the one-third octave bands by the number of bands in $\Delta f = 20$ Hz. The effectiveness of comparing predictions to experiments in this way is limited at the higher frequencies, especially where BVS noise is thought to be (between 20 and 30 kHz). Furthermore, the motor noise at 20 kHz, as well as additional tonal content surrounding the LBLVS regions, affects the one-third octave representation of the experimental data. Additionally, the low frequency broadband noise at frequencies between 1 kHz $\leq f \leq$ 10 kHz still has tonal content present in all cases; a one-third octave comparison would hide this additional content.

1. Rough Blade

First, broadband noise predictions are presented for the rough-textured blade in Fig. 22, at the $\Theta_{tip} = 7°$, $\Omega_c = 5465$ RPM condition. For these predictions, the trip flag was set to "tripped", due to the rough surface quality of the blade. Two predictions are presented, one with BVS noise and one without, in Fig. 22(a). BVS is a high frequency noise source, and is highly sensitive to the blade geometry parameters of bluntness thickness (H) and trailing edge angle (Ψ). For such small blades, these parameters can be hard to define, but as described in Section III.C.4, a bluntness thickness value of H = 0.8 mm collapsed the data appropriately for the Strouhal value of interest. The trailing edge angle (Ψ) was set to 16 degrees for these predictions. Figure 22(a) shows that both predictions match the low frequency content well, and by including BVS noise, the prediction better matches the high frequency shelf at 13 kHz, though it does overshoot in amplitude and frequency. However, the prediction that includes BVS seems to match the experimental spectral shape better. Figure 22(b) shows the self-noise sources that make up the broadband noise prediction with BVS included. Turbulent boundary layer trailing edge noise on the suction side of the blade dominates at frequencies up until approximately 8 kHz. At this point, BVS dominates the noise spectra. A fully tripped prediction seems to model the behavior of the rough blade spectra well, though the BVS noise source is not quite capturing the correct amplitudes and frequencies.

2. Smooth Blade

The smooth blade tests provide data in which LBLVS is present. Figure 23(a) shows a comparison of the experimental baseline case to three different BARC predictions: one with a tripped boundary layer condition, one with an untripped boundary layer condition and one with the inclusion of LBLVS. A tripped boundary layer condition overpredicts the noise amplitudes at the frequencies between 1 kHz $\leq f \leq$ 10 kHz, but overpredicts the noise amplitudes at frequencies higher than 10 kHz. Even though the rotor is physically smooth, an untripped boundary layer setting does not capture the separation and suction noise that occurs between 1 kHz $\leq f \leq$ 5 kHz. With the inclusion of LBLVS in the untripped prediction, LBLVS is greatly overpredicted in amplitude and frequency and dominates the spectra at most frequencies. While experimental broadband noise at low frequencies matches the trend behavior of the tripped boundary layer prediction, the content between 10 kHz and 30 kHz behaves as LBLVS (as shown by the spectral scaling trends of the experiment). So, it was attempted to partially trip the last 5% portion of the blade, as a portion of the blade may be experiencing a tip vortex roll-up that is impinging inboard, creating a boundary layer that behaves tripped up to a certain distance inboard. High-fidelity simulations are performed in an accompanying paper [3], which indicate tip vortex spillage acting on approximately 5% of the blade span, further confirming a partially tripped condition. Additionally, it is known for rotorcraft that there is an effective blade area responsible for thrust generation correspondent to approximately 95% of the original blade span, accounting for the tip vortex [7]. Predictions with this partial trip setting are presented in Fig. 23(b). The 95% untripped prediction still overpredicts the LBLVS contribution, but the low frequency noise levels match those of the experiment better. To improve LBLVS prediction, additional limiting of the laminar boundary layer mechanism by Reynolds number was also employed. A prediction limiting LBLVS to regions of the blade with

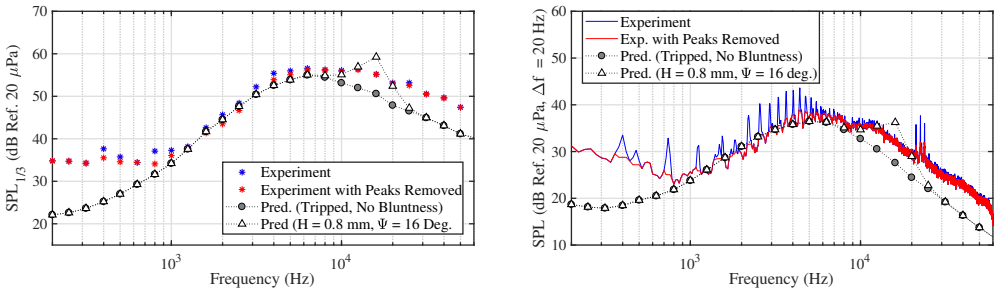

(a) Comparison of broadband noise predictions with experiment. Spectra are shown in one-third octave bands and narrowband frequencies.

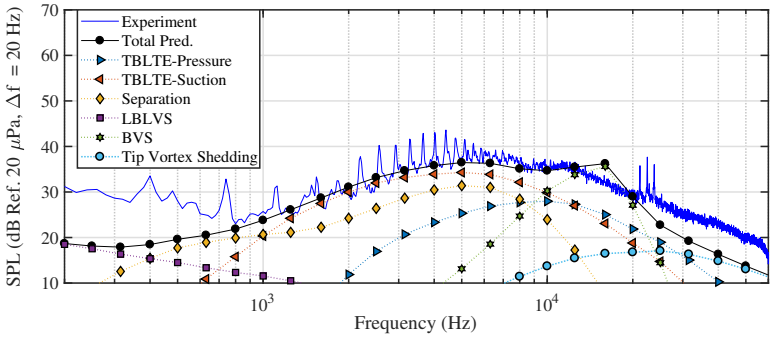

(b) Self-noise source breakdown for the fully tripped prediction.

Fig. 22 Self-noise predictions for the baseline case (Θ_{tip} = 7°, Ω_c = 5465 RPM) for the rough blade set experiment. For these predictions, bluntness thickness H was set to 0.8 mm and trailing edge angle Ψ was set to 16 degrees.

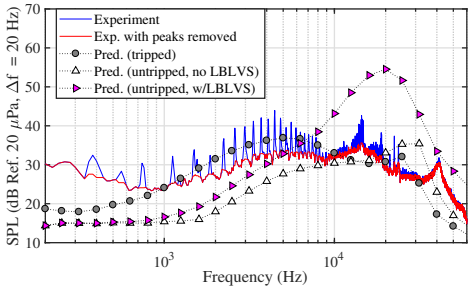

(a) Tripped and untripped predictions.

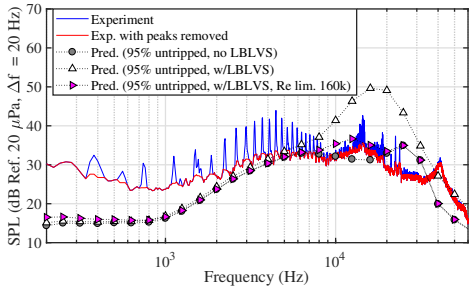

(b) Partially tripped predictions.

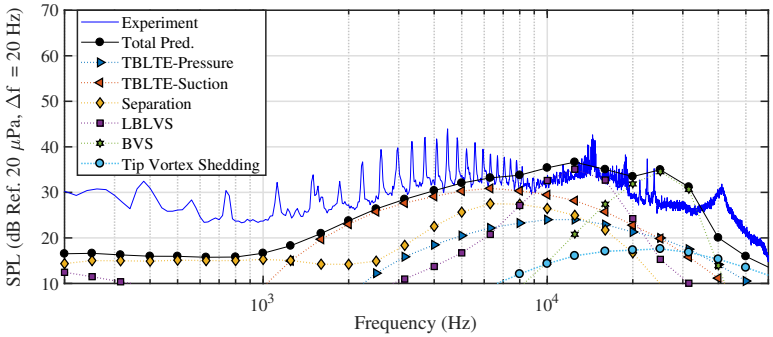

(c) Self-noise breakdown for the 95% untripped prediction, with LBLVS limited to regions of the blade with Re < 160, 000.

Fig. 23 Self-noise predictions for the baseline case (Θ_{tip} = 7°, Ω_c = 5510 RPM) for the smooth blade set experiment. For these predictions, bluntness thickness H was set to 0.5 mm and trailing edge angle Ψ was set to 14 degrees.

Reynolds number less than 160,000 is also shown in Fig. 23(b). Using this partially tripped, Reynolds number limited prediction, the various self-noise mechanisms as predicted by BARC are broken down in Fig. 23(c). The TBLTE noise on the suction side of the airfoil is responsible for the low frequency noise in the prediction. BVS is overpredicted in these predictions in both amplitude and frequency. The self-noise predictions are highly sensitive to the defined boundary layer conditions. A partially tripped, Reynolds number limited prediction roughly captures the shape of the smooth blade experiment, but over- and underpredicts the noise amplitudes at the various frequencies.

For the low rotation rate condition, Fig. 24(a) presents a comparison of two predictions: one fully untripped and one with a partial trip at 95%. The fully untripped prediction overpredicts the amplitude at frequencies higher than 8 kHz; however, it matches the frequency peak very well. The 95% untripped prediction matches the experimental trend very well in both amplitude and frequency, with the exception of underpredicting low frequency noise. For these predictions, H was set to 0.5 mm and Ψ was set to 14 degrees. Bluntness parameters were difficult to set to match what is believed to be bluntness noise at 15 kHz, though this could be due to this frequency falling between one-third octave frequencies. The source breakdown of the 95% untripped prediction is seen in Fig. 24(b). For this low rotation rate condition, LBLVS is the pronounced noise source in the prediction. TBLTE noise on the suction side of the airfoil is predicted to dominate at the frequencies between 1.25 kHz $\leq$ f $\leq$ 4 kHz. BVS noise is predicted to appear at the higher frequency range between 10 kHz $\leq$ f $\leq$ 16kHz.

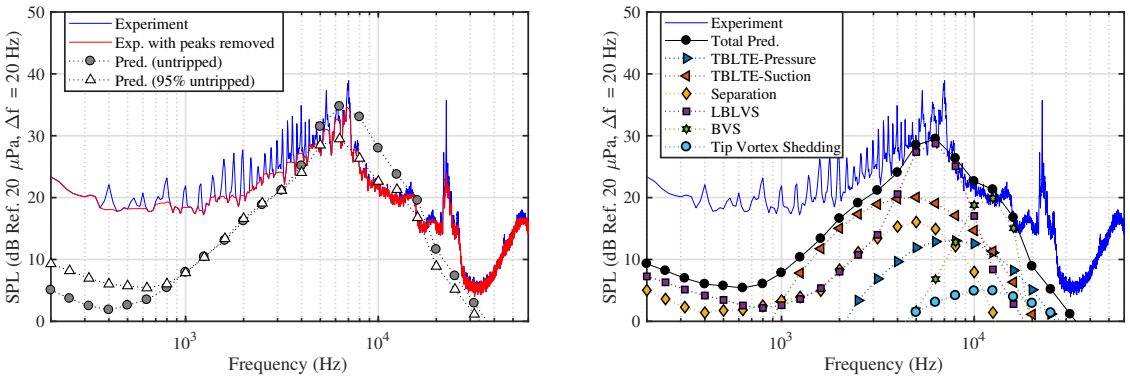

(a) Untripped and partially tripped predictions

(b) Self-noise breakdown for the 95% untripped prediction

Fig. 24 Self-noise predictions for the low rotation rate case (Θ_{tip} = 7°, Ω_c = 2938 RPM) for the smooth blade set experiment. For these predictions, bluntness thickness H was set to 0.5 mm and trailing edge angle Ψ was set to 14 degrees.

Finally, Fig. 25 shows the low tip pitch prediction comparisons to the experiment. For this case, even a Reynolds number limit of 160,000 did little in suppressing LBLVS appropriately, as seen in Fig. 25(a). A Reynolds number limit of 135,000 was also implemented, but this reduced the frequency of the LBLVS prediction to lower values than expected. Thus, for this condition, the LBLVS prediction is inadequate, even when applying the Reynolds number limit. However, using the uniform inflow model in ROTONET to calculate the local inflow conditions may not be adequate for off-design tip pitch conditions such as this one. The prediction of this noise source is highly sensitive to local angle attack, and the simplified uniform inflow model may not be sufficient for this case. It is possible that the original Reynolds number limit of 160,000 may produce a decent prediction if used with a more accurate local angle of attack, as LBLVS would not develop as strongly. The rest of the spectrum seems to be captured well, using trailing edge bluntness parameters of H = 0.5 mm and Ψ = 18 degrees. A source breakdown of the prediction with the Reynolds number limit of 135,000 is shown in Fig. 25(b).

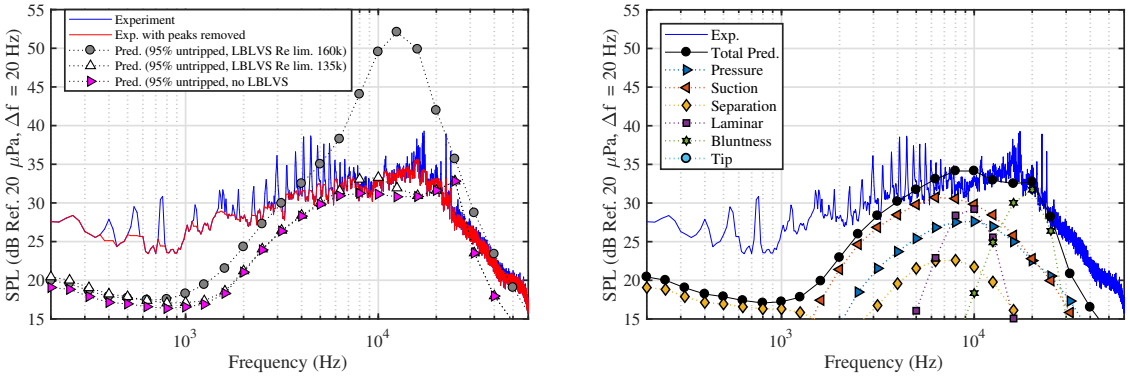

(a) Effect of boundary layer settings on predictions.

(b) Self-noise breakdown for the 95% untripped prediction with Reynolds number limit of 135,000.

Fig. 25 Self-noise predictions for the low tip pitch case (Θ_{tip} = 4°, Ω_c = 5535 RPM) for the smooth blade set experiment. For these predictions, bluntness thickness H was set to 0.5 mm and trailing edge angle Ψ was set to 18 degrees.

F. Comments

- The prediction of BVS is dependent on bluntness thickness H and trailing edge angle Ψ. The choice for trailing edge angle is a bit arbitrary, which has been the case for previous predictions [23]. Because these blades are so small, the exact printed bluntness thickness is difficult to ascertain. Based upon spectral scaling and noise trends, bluntness noise is identified in the experiment; however, the predictions tended to overpredict the amplitude and frequency of this noise source with initial bluntness value settings. The prediction method of Ref. [18] is a one-third octave prediction method, and at these high frequencies at which BVS is found, it is difficult to make a comparison between the experiment and data (especially since motor noise is present at 23 kHz). Though matching the amplitude and frequency of the BVS noise prediction to that of the experiment was challenging, the spectral scaling analysis of the experimental data confirms that it is present in all cases.
- Laminar bluntness vortex shedding was a noise source identified in the experiments, and predictions are generally able to capture the frequency at which this mechanism peaks. However, it is apparent that the amplitude of LBLVS is overpredicted by this prediction method. By partially tripping the outermost 5% of the blade and imposing a local Reynolds number limit, predictions match experiments better for some cases.
- The broadband noise comparisons made in this section are under the assumption that self-noise is the primary culprit for the broadband noise. Turbulence ingestion noise and blade wake interaction noise were identified in Ref. [3], and an underprediction of noise below 10 kHz is expected with the current toolset. In other words, techniques like partial-tripping may in fact be emulating the effect of BWI and/or TIN, as potentially evidenced in Ref. [3].

IV. Conclusions

The experiments conducted in the SHAC provided a data set for a rotor with an ideal twist distribution. Acoustic and performance data were collected for the ideally twisted rotor with smooth surface blades at three tip pitch conditions. The ideally twisted rotor did not match performance expectations when tested in the SHAC, though this is thought to be due to tip loss effects not modeled in the design process. After examining the spectra for the different test conditions, broadband noise was found to have a dominant contribution, and there was apparent noise at various frequencies. The baseline case provided spectra that were free from effects of background noise and motor noise, but the low rotation rate case provided higher levels of the noise sources at the frequencies in question. Because of this, acoustic trends were identified for the rotational sweep and blade tip pitch conditions.

For the high and mid blade tip pitch conditions, it was observed that a high frequency residual noise mechanism was present that is currently not identified. While it could be tip vortex shedding, it could also be turbulence surrounding the tip, as this noise is most prominent at the higher tip speeds. Spectra were scaled with tip speeds, and the frequencies were scaled with the Strouhal number with bluntness length as the length scale. By scaling spectra using trailing edge bluntness length and tip Mach number, it was possible to see the frequency ranges where broadband noise is either

not scaling with rotation rate, or indicative of a laminar to turbulent boundary layer transition behavior. Additionally, spectral amplitude collapse around the Strouhal number of 0.1 indicated BVS being present in all cases.

After an assessment of the experimental spectra, low fidelity tools were tested against the experiments. For this paper, broadband noise prediction was limited to self-noise prediction, and did not include additional broadband noise sources such as blade wake interaction or turbulence ingestion. The results of an accompanying paper [3] investigate these noise sources with a lattice-Boltzmann method solver, and indicate that these mechanisms have an important contribution to the overall system broadband noise. The self-noise mechanisms identified in this study were LBLVS, BVS and TBLTE noise. LBLVS is present for the smooth-textured ideally twisted rotor at all rotation rates, but more prominent at the lower tip speeds. While low-fidelity predictions are capable of reasonably predicting the tonal and broadband noise content for some testing conditions, they required limits on LBLVS and modifications to the trailing edge geometry. It is clear that broadband noise generation is highly dependent on boundary layer transition along the blade as well as secondary effects due to tip vortex generation. LBLVS is a noise source that is especially sensitive to boundary layer conditions that change along the span of the blade.

It is suspected that varying tip pitch significantly changes the noise sources and inflow conditions, therefore, additional predictions are warranted that would incorporate the use of an aerodynamic modeling tool with nonuniform inflow modeling options such as CAMRAD II (Comprehensive Analytical Model of Rotorcraft Aerodynamics and Dynamics[24]). While not presented in this paper, the semiempirical method is present in the ANOPP2 Self Noise Internal Functional Module (ASNIFM), which can be used with the rest of the ANOPP2 suite to characterize and predict the noise impact of full vehicle designs.

Acknowledgments

The authors thank the NASA Revolutionary Vertical Lift Technology (RVLT) project and the NASA Langley Center Innovation Fund for Internal Research and Development (CIF-IRAD) for funding this work. The authors thank Siena Whiteside who led the effort of the Aeronautics Systems Analysis Branch in design and printing of the blades used in this experiment. Beau Pollard and Xiaofan Fei designed the 3-D blades, and Shali Subramanian aided in both manufacturing and testing the blades in the SHAC. Finally, the LSAWT team (John Swartzbaugh, Stan Mason, Jeff Collins, Bryan Lamb and Mick Hodgins) helped with testing in the SHAC.

References

[1] Whiteside, S., Zawodny, N., Fei, X., Pettingill, N. A., Patterson, M. D., and Rothhaar, P., "An Exploration of the Performance and Acoustic Characteristics of UAV-Scale Stacked Rotor Configurations," AIAA Scitech 2019 Forum, San Diego, CA, AIAA Paper 2019-1071, Jan 2019.

[2] Zawodny, N. S., Boyd Jr., D. D., and Burley, C. L., "Acoustic Characterization and Prediction of Representative, Small-Scale Rotary-Wing Unmanned Aircraft System Components," 72nd American Helicopter Society Annual Forum, 2016.

[3] Thurman, C. S., Zawodny, N. S., Pettingill, N. A., and Lopes, L. V., "Physics-informed Broadband Noise Source Identification and Prediction of an Ideally Twisted Rotor," 2021 SciTech Forum, Nashville, TN, Jan. 2021.

[4] Pettingill, N. A., and Zawodny, N. S., "Identification and Prediction of Broadband Noise for a Small Quadcopter," Vertical Flight Society International 75th Annual Forum & Technology Display, Philadelphia, PA, May 2019.

[5] Lopes, L. V., and Burley, C., ANOPP2 User's Manual: Version 1.2, Hampton, VA, NASA/TM-2016-219342.

[6] Burley, C. L., and Brooks, T. F., "Rotor Broadband Noise Prediction with Comparison to Model Data," Journal of the American Helicopter Society, Vol. 49, No. 1, 2004, pp. 28–42.

[7] Leishman, J. G., Principles of Helicopter Aerodynamics, 2nd ed., chapter and pages, pp. 87–113.

[8] MarkForged, "Onyx," , 2020. URL https://markforged.com/materials/plastics/onyx.

[9] MarkForged, "MarkForged X7 3D Printer," , 2020. URL https://markforged.com/3d-printers/x7.

[10] Protolabs, "Proto Labs, Inc." , 2020. URL https://www.protolabs.com/.

[11] Protolabs, "Stereolithography ABS-Like White Material Data Sheet," , December 2019. URL https://www.protolabs.com/media/1019519/sla-data-sheet-accura-xtremewhite200-f.pdf.

[12] Protolabs, "Selective Laser Sintering PA 12 Mineral-Filled Material Data Sheet," , June 2019. URL https://www.protolabs.com/media/1019529/sls-data-sheet-pa-12-mineral-filled-f.pdf.

[13] varioPROP, "varioPROP," , 2020. URL http://www.ramoser.de/home_e/varioprop_e/varioprop_e.html.

[14] Stephenson, J. H., Weitsman, D., and Zawodny, N. S., "Effects of flow recirculation on unmanned aircraft system (UAS) acoustic measurements in closed anechoic chambers," The Journal of the Acoustical Society of America, Vol. 145, No. 3, 2019, pp. 1153–1155. https://doi.org/10.1121/1.5092213, URL http://dx.doi.org/10.1121/1.5092213.

[15] Nguyen, L. C., and Kelly, J. J., A Users Guide for the NASA ANOPP Propeller Analysis System, Hampton, VA, 1997. NASA CR 4768.

[16] Weir, S. D., Jumper, J. S., Burley, C. L., and Golub, A. R., "Aircraft Noise Prediction Program Theoretical Manual: Rotorcraft System Noise Prediction System (ROTONET), Part 4," NASA TM 83199, April 1995.

[17] Brooks, T. F., Marcolini, M. A., and Pope, D. S., "Main Rotor Broadband Noise Study in the DNW," Journal of the American Helicopter Society, Vol. 34, No. 2, 1989, pp. 3–12.

[18] Brooks, T. F., Pope, D. S., and Marcolini, M. A., "Airfoil Self-Noise and Prediction," NASA RP 1218, 1989.

[19] Brooks, T. F., and Burley, C. L., "Blade Wake Interaction noise for a main rotor," Journal of the American Helicopter Society, Vol. 49, No. 1, 2004, pp. 11–27. https://doi.org/https://doi.org/10.4050/JAHS.49.11.

[20] Amiet, R. K., Noise Produced by Turbulent Flow Into a Rotor: Theory Manual for Noise Calculation, East Hartford, CT, NASA CR 181788, 1989.

[21] Zawodny, N. S., and Boyd Jr., D. D., "Investigation of Rotor-Airframe Interaction Noise Associated with Small-Scale Rotary-Wing Unmanned Aircraft Systems," 73rd American Helicopter Society Annual Forum, 2017.

[22] Brentner, K., and Farassat, F., "Modeling aerodynamically generated sound of helicopter rotors," Progress in Aerospace Sciences, Vol. 39, 2003, pp. 83–120. https://doi.org/10.1016/S0376-0421(02)00068-4, URL http://linkinghub.elsevier.com/retrieve/pii/S0376042102000684.

[23] Brooks, T. F., Marcolini, M. A., and Pope, D. S., "Main Rotor Broadband Noise Study in the DNW," Journal of the American Helicopter Society, Vol. 34, No. 2, 1989, pp. 3–12.

[24] Johnson, W., "A General Free Wake Geometry Calculation For Wings and Rotors," American Helicopter Society 51st Annual Forum, Fort Worth, Texas, 1995.